Magnetic dynamics and spin-phonon coupling in the antiferromagnet Ni_2NbBO_6

M. A. Prosnikov,* A. N. Smirnov, V. Yu. Davydov, and R. V. Pisarev
Ioffe Institute, Russian Academy of Sciences, 194021 St.-Petersburg, Russia

N. A. Lyubochko and S. N. Barilo
Institute of Solid State and Semiconductor Physics, National Academy of Sciences, 220072 Minsk, Belarus

(Received 19 March 2018; revised manuscript received 4 May 2018; published 4 September 2018)

Antiferromagnetic systems with rich spin dynamics and pronounced interplay between magnetic and lattice degrees of freedom are of great interest in the emerging field of terahertz and subterahertz magnonics and spintronics. Here we report on spin and lattice dynamics of single crystals of Ni_2NbBO_6 studied with the use of polarized Raman spectroscopy in the temperature range of 10–300 K which includes the antiferromagnetic transition at $T_N = 23.5$ K. Well-defined and highly polarized magnetic excitations were observed below and partly above T_N. Three magnetic modes at 30, 84, and 113 cm^{-1} (at $T = 10$ K) were detected. The two high-energy magnetic excitations were identified as two-magnon modes. In total, 57 out of the expected 60 Raman-active phonons were registered and identified. Several modes revealed a nontrivial spin-phonon coupling manifesting either hardening or softening mostly below T_N. The possible magnetic space groups were determined through symmetry analysis. Spin-wave spectra and density of states were calculated within the linear spin-wave theory for supporting the experimental findings.

DOI: 10.1103/PhysRevB.98.104404

I. INTRODUCTION

Complex magnetics with various types of superexchange connectivity are of great interest because they demonstrate nontrivial physical properties covering both classical and quantum magnetism. Some examples are low-dimensional fully and partly dimerized systems [1], integer spin-Haldane magnets [2,3], Kitaev magnetics [4–6], frustrated spin-ice magnets [7], kagome lattices [8,9], and many others [10]. Each of the mentioned systems may possess various kinds of admissible spin-related excitations such as one and multi-magnons, spin-gap dimers, and magnetic bound states [1,11]. The observation of these modes provides an opportunity to get deeper insight into the ground and excited states and phases, and determine the anisotropy and exchange constants, sometimes in exotic biquadratic and four-spin forms [12].

It should be mentioned that besides the fundamental interest to these systems, in the last few years, within the fields of magnonics and spintronics, the attention notably shifted from ferromagnets toward antiferromagnets as very promising materials. This trend was motivated by several advantages of antiferromagnets, such as the negligible spin-dipole interaction, the ability to convert electron spin current to a magnonic one [13–15], the spin superfluidity [16], and, as a rule, richer magnetic dynamics in a much wider spectral range up to several terahertz [17,18]. The antiferromagnetic magnonics and spintronics thus became a rapidly developing field with potentially important practical applications [19,20].

Richness and complexity of spin excitations in antiferromagnets require application of various complementary experimental techniques such as terahertz and infrared spectroscopy, inelastic neutron and resonant x-ray inelastic scattering, impulsive stimulated Raman scattering [21], and others. In comparison to the large-scale facilities, the table-top Raman-scattering spectroscopy is a powerful, versatile and sensitive tool for investigating nearly all possible types of collective excitations, as well as the interplay of charge, spin, orbital and lattice degrees of freedom [22,23]. The magnetic light scattering can also provide information about exchange paths and coupling constants, spinon excitations, spin gaps [1,24], and a variety of perturbations of a magnetic system [25]. Moreover, considering the fine energy resolution ($\approx$1 cm^{-1} $\approx$0.1 meV) and the possibility to work with small-size samples, the Raman spectroscopy is a well recognized technique for studying spin dynamics of 3*d* and other magnetics [26]. Recently, two-magnon Raman scattering was observed in 5*d* compounds [27,28], providing insights into the nontrivial magnetic physics of such systems.

A magnetic insulator dinickel niobium boron oxide Ni_2NbBO_6 with complex structural and magnetic connectivities has been known for quite a long time [29] but up to now its dynamical properties remain practically unexplored. The crystal structure was determined in Ref. [30] by the means of x-ray diffraction. It was found that, from a structural point of view, Ni_2NbBO_6 consists of zigzag chains of edge-shared distorted [NiO_6] and [NbO_6] octahedra cross-linked through corner-shared [BO_4] tetrahedra. Low-temperature absorption measurements in the spectroscopic range 5000–28 000 cm^{-1} were presented in Ref. [31]. Four groups of absorption bands associated with electronic transitions with single and multi-phonon sidebands located at 6800–10 500, 11 500–18 000, 19 000–22 000, and 22 000–26 500 cm^{-1} were registered at 4.2 K. Positions of the main bands were interpreted through

*yotungh@gmail.com

ligand-field theory and compatible with reduction of Ni^{2+} site symmetry according to the following scheme $m\bar{3}m(O_h) \rightarrow 3m(C_{3v}) \rightarrow m(C_s) \rightarrow 1(C_1)$, with a large cubic crystal field splitting $\Delta = 8300$ cm^{-1}. Single crystal growth, structure refinement, magnetostatic properties, and *ab initio* calculations of the magnetic ground state of Ni_2NbBO_6 were recently published in Ref. [32]. The establishment of a long-range three-dimensional (3D) antiferromagnetic (AFM) phase at $T_N = 23.5$ K with the AFM vector lying along the a axis as well as spin-flop transition at $\mu_0 H_{sf} = 3.67$ T were observed. The density functional theory (DFT) calculations point out a ground state of FM/AFM alternating armchair chains running along the b axis. Such chains are ferromagnetically coupled, forming the 3D AFM state.

In this paper, we report on a comprehensive experimental study of the spin and lattice dynamics of Ni_2NbBO_6 with the use of the polarized Raman spectroscopy in a broad temperature range including $T_N = 23.5$ K. Direct measurements of phonon and spin excitations are a valuable source of information about lattice and spin dynamics and their interactions. Experimental results are supported by theoretical investigation carried out through magnetic symmetry analysis and a linear spin wave theory (LSWT) approach. The rich set of obtained data has been used for evaluating exchange and anisotropy constants and suggesting an alternative magnetic structure thus providing more a reasonable and deeper understanding of the static and dynamic properties of Ni_2NbBO_6.

The paper is organized as follows. Section II describes the growth of single crystals and experimental technique. In Sec. III the crystal structure is described. Discussion of the phonon modes symmetry is followed by a presentation and analysis of experimental results on the lattice dynamics and spin-phonon effects. Magnetic structure, symmetry, and spin dynamics with interpretation and theoretical models are given in Sec. IV. Section V summarizes experimental and theoretical results and ends with the conclusions.

II. EXPERIMENTAL DETAILS

A. Samples

Single crystals of Ni_2NbBO_6 have been grown by the flux-melt technique, following a procedure described in [29]. Dried $Na_2B_4O_7$ and up to 40% excess of Nb_2O_5 as a solvent were used. A sawlike cooling-temperature profile allowed us to limit the number of nuclei during crystallization. Synthesized crystals were of a typical size $\approx 1 \times 1 \times 0.5$ mm characterized by the light-green color, specific for many crystals with Ni^{2+} ions in octahedral oxygen O^{2-} coordination. A "green" transparency window around 2.3 eV is a characteristic feature observed in NiO and other nickel oxides [33–36]. All samples used for experiments were twin-free according to our polarized microscopy and Raman spectroscopy measurements. Part of the scattering experiments were performed on natural as-grown faces. Other crystals were cut and optically polished allowing us to obtain samples providing all required geometries. The orthorhombic setting of the axes was adopted from Refs. [30,32] (see Table I).

TABLE I. Crystal-structure parameters of Ni_2NbBO_6.

Space group #62 *Pnma* (D_{2h}^{16})	Ion type and Wyckoff position	Reduced coordinates[a] x	y	z
$a = 10.057$ Å[a]	Ni (8*d*)	0.13554	0.07020	0.48139
$b = 8.618$ Å[a]	Nb (4*c*)	0.41866	0.25000	0.47239
$c = 4.490$ Å[a]	O1 (4*c*)	0.22711	0.25000	0.23020
$V = 389.2$ Å^3 [a]	O2 (4*c*)	0.08431	0.25000	0.78263
$a = 10.0690$ Å[b]	O3 (8*d*)	0.29239	0.38483	0.76158
$b = 8.6266$ Å[b]	O4 (8*d*)	−0.03806	0.41537	0.25840
$c = 4.4932$ Å[b]	B (4*c*)	0.22646	0.25000	0.91060

[a]Reference [30].
[b]Reference [32].

B. Raman spectroscopy

Raman scattering spectra were measured in the range of 10–1100 cm^{-1} with the use of a T64000 (Jobin-Yvon) spectrometer in the triple monochromator subtraction mode equipped with 1800 lines/mm diffraction gratings and a liquid-nitrogen-cooled CCD camera. The 532 nm (2.33 eV) line of a Nd:YAG laser (Torus; Laser Quantum, Inc.) with appropriate interference filter was used as the excitation source. A 50× objective was employed both to focus the incident beam and to collect the scattered light. Temperature-dependent measurements were done in the energy region of 12–620 cm^{-1} and in the temperature range of 10–250 K. Low-temperature spectra were recorded using a helium closed-cycle cryostat (Cryo Industries, Inc.) with temperature stability better than 1 K. Silver paste was used for mounting single crystals on the cryostat cold finger. Calibration of the spectrometer was done with the 520.7 cm^{-1} phonon line of a Si single crystal. All measurements were done in the backscattering geometry for all informative polarization settings, labeled with the use of the Porto notation where a, b, and c directions coincide with the crystallographic axes. For example, $a(bc)\bar{a}$ stands for the case where the incident light, linearly polarized along the b axis, propagates and backscatters along the same a axis, while the component of scattered light with the polarization along the c axis is measured.

III. LATTICE DYNAMICS

A. Crystal structure and phonon modes

Ni_2NbBO_6 belongs to the *norbergite* orthorhombic structure characterized by a *mmm* point group and a *Pnma* (#62, $Z = 8$) space group [37]. Crystal cell parameters are listed in Table I according to Refs. [30,32]. The structure consists of [NiO_6] and [NbO_6] octahedral and [BO_4] tetrahedral groups, as shown in Fig. 1. In Ni_2NbBO_6, the magnetic Ni^{2+} ions ($3d^8$, $S = 1$) occupy only the general 8*d* positions (site symmetry 1), whereas diamagnetic Nb^{5+} ions occupy only the 4*c* positions (site symmetry *.m.*).

The symmetry analysis of the crystal unit cell of Ni_2NbBO_6 yields 120 phonon modes in total [see Eq. (1)]. These are 60 even Raman-active modes ($17A_g + 13B_{1g} + 17B_{2g} + 13B_{3g}$), 44 odd infrared modes ($16B_{1u} + 12B_{2u} + 16B_{3u}$), 13 "silent" modes A_u inactive in both processes, and three acoustic ones ($1B_{1u} + 1B_{2u} + 1B_{3u}$). Hereafter, further consideration will

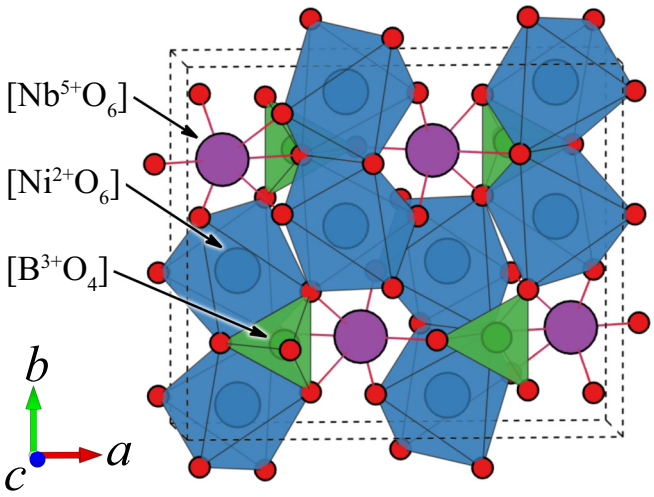

FIG. 1. Polyhedra representation of the crystal structure of Ni_2NbBO_6. Structural elements [NiO_6] and [NbO_6] octahedra, and [BO_4] tetrahedra are depicted by different colors. Thin dashed lines represent the single unit cell.

be focused on the even modes, and the corresponding Raman tensors are shown in Eq. (2).

$$\Gamma = 17A_g + 13B_{1g} + 17B_{2g} + 13B_{3g} + 13A_u + 17B_{1u} + 13B_{2u} + 17B_{3u}. \quad (1)$$

It is seen that A_g modes should be observed in all diagonal incident-scattered polarizations. However, these modes may have different, and even vanishing, intensity in each particular polarization due to the nonequivalence of diagonal tensor elements. In its turn, B_{1g}, B_{2g}, and B_{3g} modes can be detected only in mutually exclusive combinations of crossed polarizations.

$$A_g = \begin{pmatrix} a & 0 & 0 \\ 0 & b & 0 \\ 0 & 0 & c \end{pmatrix}, \quad B_{1g} = \begin{pmatrix} 0 & d & 0 \\ d & 0 & 0 \\ 0 & 0 & 0 \end{pmatrix},$$
$$B_{2g} = \begin{pmatrix} 0 & 0 & e \\ 0 & 0 & 0 \\ e & 0 & 0 \end{pmatrix}, \quad B_{3g} = \begin{pmatrix} 0 & 0 & 0 \\ 0 & 0 & f \\ 0 & f & 0 \end{pmatrix}. \quad (2)$$

B. Lattice scattering

As discussed above, 60 Raman-active phonons of different symmetries are expected in Ni_2NbBO_6 and for distinguishing them, measurements were done using the complete set of incident-scattered polarizations. As a result, most of the expected phonons were detected. Since the number of phonons is large, it was more informative to study the spectra at low temperature due to the increased intensity of phonons and greatly reduced halfwidths. Figure 2 shows the measured spectra at 10 K for all six required polarizations. Small leaks of forbidden modes were observed due to practically inevitable depolarization in optical elements and a small misalignment of the light polarization with respect to the crystallographic axes. Nevertheless, the analysis of the full set of obtained polarized spectra made it possible to reliably determine the symmetry of each particular mode. Nonequivalence of the diagonal Raman-tensor elements being a general feature inherent to orthorhombic systems [see Eq. (2)] leads to unequal

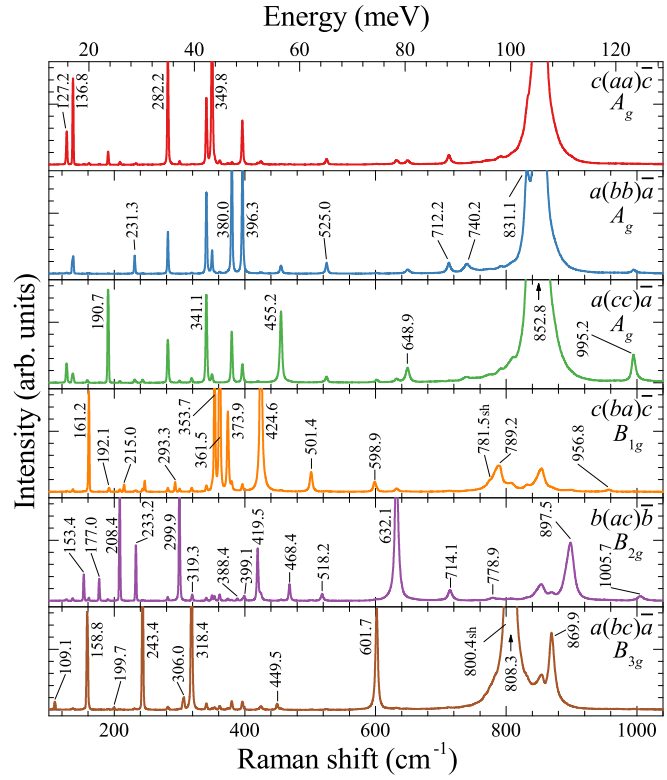

FIG. 2. Raman scattering spectra of Ni_2NbBO_6 at $T = 10$ K for selected polarizations featuring phonon modes of all allowed symmetries. Numbers represent experimentally registered phonon frequencies of the most intense lines.

intensities for the A_g modes in different diagonal polarizations. Phonon frequencies, intensities, and full widths at half maxima (FWHMs) were extracted by fitting the Raman spectra to the Voigt profiles [38] within the FITYK code [39] with a typical R-squared value above 0.98. Derived parameters at $T = 10$ K are listed in Table II. The lowest frequency mode is the B_{3g} one at 109.1 cm^{-1}, while the B_{2g} mode at 1005.7 cm^{-1} has the highest frequency. The most intense A_g mode at 852.8 cm^{-1} evidently corresponds to stretching of the [BO_4] groups, falling within the range of 740–890 cm^{-1} [40].

In total, 57 out of the 60 predicted phonon modes were registered. We note that in the isostructural ferroborate Fe_3BO_6, only 39 out of 60 phonons were observed [41]. A comparison shows that the phonon spectra of both these crystals are similar in their general features, due to their structural and compositional similarities. We also note that no emergence of new phonons was observed in Ni_2NbBO_6 down to 10 K, which proves the absence of any structural phase transition.

Detailed studies of temperature dependences of phonon frequencies showed their nontrivial behavior slightly above and below the AFM transition temperature. The phonon frequencies and FWHMs were fitted in the temperature range 40–250 K applying the (3+4)-phonon anharmonic model [42,43]:

$$\omega_i(T) = \omega_i(0) - A\left(1 + \frac{2}{e^{hc\omega_{i0}/2k_BT} - 1}\right) - B\left(1 + \frac{3}{e^{hc\omega_{i0}/3k_BT} - 1} + \frac{3}{(e^{hc\omega_{i0}/3k_BT} - 1)^2}\right), \quad (3)$$

TABLE II. Symmetry, number of observed/predicted modes with frequency (cm^{-1}), and FWHM (cm^{-1}) at $T = 10$ K.

A_g 17/17		B_{1g} 13/13		B_{2g} 16/17		B_{3g} 11/13	
Freq.	FWHM	Freq.	FWHM	Freq.	FWHM	Freq.	FWHM
127.2	1.7	161.2	1.5	153.4	1.6	109.1	2.0
136.8	1.5	192.1	2.0	177.0	1.7	158.8	2.1
190.7	1.9	215.0	1.7	208.4	1.6	199.7	2.2
231.3	1.7	293.3	1.7	233.2	1.6	243.4	2.1
282.2	1.8	353.7	2.0	299.9	1.8	306.0	2.9
341.1	2.5	361.5	2.3	319.3	2.1	318.4	2.5
349.8	2.0	373.9	2.7	388.4	2.0	449.5	2.9
380.0	1.9	424.6	4.2	399.1	2.6	601.7	4.4
396.3	2.0	501.4	4.6	419.5	2.5	800.4	8.4
455.2	4.0	598.9	5.4	468.4	2.7	808.3	10.8
525.0	3.9	781.5	18.4	518.2	3.8	869.9	11.2
648.9	6.6	789.2	10.3	632.1	6.2		
712.2	6.0	956.8	8.5	714.1	8.7		
740.2	11.1			778.9	11.5		
831.1	6.1			897.5	14.4		
852.8	10.9			1005.7	11.7		
995.2	7.0						

where i is the index of the phonon mode, $\omega_i(0)$ is the zero-temperature frequency of a corresponding mode in absence of spin-phonon interaction, k_B is the Boltzmann constant, and T stands for temperature. A and B constants represent three- and four-phonon anharmonic contributions, respectively.

The FWHM dependence can be written in the same manner as

$$\Gamma_i(T) = \Gamma_i(0) + C\left(1 + \frac{2}{e^{hc\omega_{i0}/2k_BT} - 1}\right) + D\left(1 + \frac{3}{e^{hc\omega_{i0}/3k_BT} - 1} + \frac{3}{(e^{hc\omega_{i0}/3k_BT} - 1)^2}\right), \quad (4)$$

where $\Gamma_i(0)$ is the intrinsic zero-temperature width, ω_{i0} are the same as in Eq. (3), and C and D are the constants reflecting three- and four-phonon anharmonic contributions.

Such an approach allowed us to obtain a good description of the high-temperature paramagnetic part (see Fig. 3). Values of constants for each individual curve (panels from left to right and top to bottom) are summarized in Table III. One should note that obtained values of anharmonic constants must be only regarded as estimates, since the temperature range of 10–250 K cannot provide enough data for full characterization of anharmonic contributions.

Some of the phonons showed behavior almost perfectly following anharmonic curves in the whole temperature range, as shown in the two upper plots in Fig. 3. However, several other phonons demonstrated either abrupt softening or hardening at the AFM transition. While such spin-phonon anomalies were manifested for the phonon frequencies, almost no changes were detected for FWHMs, suggesting the absence or vanishingly small contribution of spin-phonon interaction to phonon relaxation processes. It is also worth noting that a weak but noticeable effect of short-range ordering is reliably manifested as hardening or softening of the phonons even at temperatures slightly exceeding T_N.

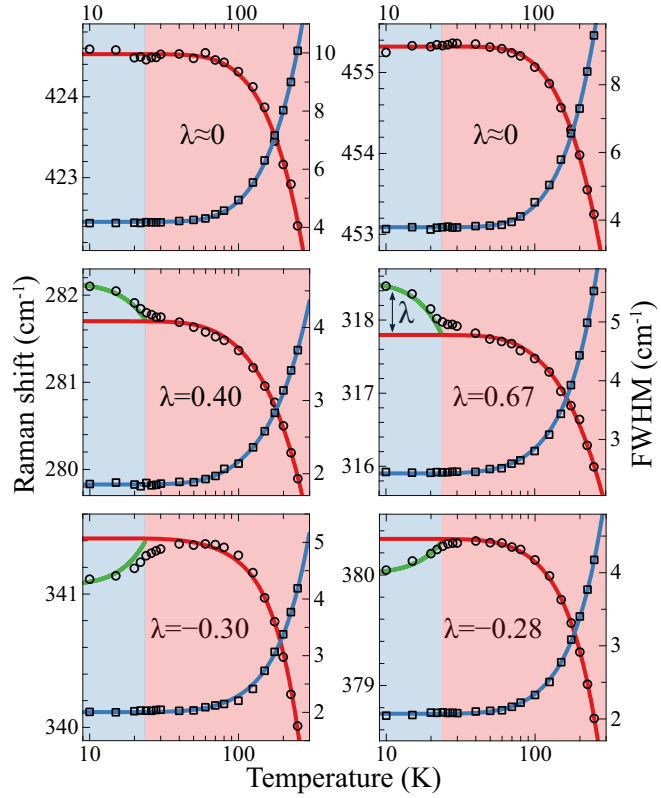

FIG. 3. Temperature dependences of phonon frequencies (circles, left axes) and FWHMs (squares, right axes) for several selected phonons in paramagnetic and antiferromagnetic phases, shown as shaded red and blue regions, respectively. Solid red and blue curves are calculated within anharmonic (3+4) phonon-relaxation approximation for frequencies and FWHMs, respectively. Brillouin-like spin-phonon contributions in magnetically ordered phase are shown as green lines; note opposite signs or the absence of any pronounced effect for different phonons.

It was shown that the contribution of spin-phonon interaction to phonon energy can be phenomenologically described by using a static spin-spin correlation average function $\lambda\langle \mathbf{S}_i \cdot \mathbf{S}_j \rangle$ for adjacent spins [44]. It is convenient to estimate the magnetic contribution to renormalization of phonon frequency within the mean-field approach as a $(\langle S^z \rangle / S)^2$, where $\langle S^z \rangle$ is calculated using the Brillouin function. Fitting of the experimental data for the case of Ni^{2+} ions with the spin $S = 1$ gives satisfactory

TABLE III. Three(A/C)- and four(B/D)-phonon anharmonic contributions to the frequencies and FWHMs of selected phonons.

$\omega_i(0)$ (cm^{-1})	A	B	$\Gamma_i(0)$ (cm^{-1})	C	D
426.09	1.34	0.22	0.56	2.78	0.84
457.95	2.56	0.06	0.92	1.64	1.22
285.54	0.78	0.05	1.11	0.67	0.08
319.11	1.19	0.03	1.74	0.34	0.33
342.56	1.13	0.00	1.46	0.27	0.27
381.79	1.56	0.00	1.42	0.33	0.32

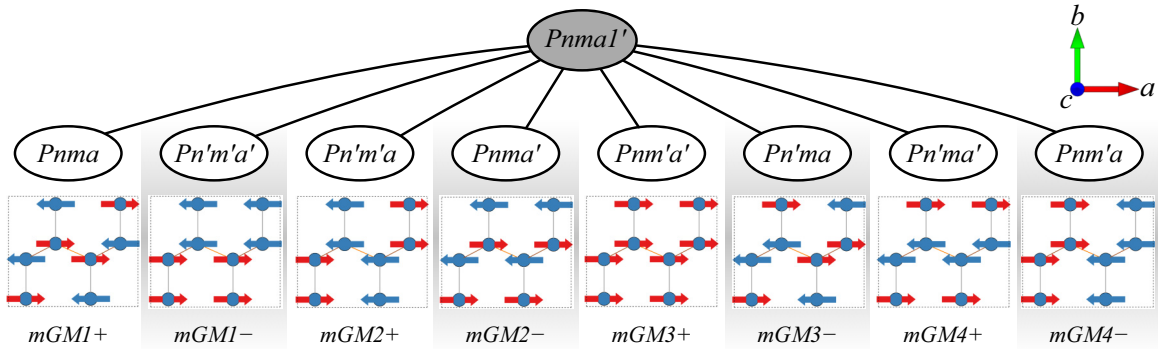

FIG. 4. Eight k-maximal magnetic subgroups with corresponding *irreps* for $\mathbf{k} = (0, 0, 0)$ propagation vector and Ni^{2+} ions in the 8d positions. Index (G:Gmag) of the each group/subgroup pair is two. Only configurations with the basis functions Ψ_x are shown.

results with spin-phonon coupling coefficients λ different for different phonons as shown in Fig. 3. It should be noted that for the $S = 1$ case the frequency shift at lowest temperature is equal to λ. In principle, spin correlation function (in the mean-field approach) should vanish in the paramagnetic region, but the manifestation of short-range ordering still can be observed even above T_N but is too small for quantitative analysis.

Striking features of the spin-phonon interaction in Ni_2NbBO_6 are phonon-frequency changes manifested in positive or negative signs of this effect, or in its complete absence depending on the particular mode as shown in Fig. 3. Frequency changes are typically small, predominantly on the order of 1 cm^{-1} and smaller. Nevertheless, they are reliably detected and fit well with the square of the $S = 1$ Brillouin function. Some exceptional examples are known, when much more prominent effects are observed, e.g., in CuO, where $\lambda \approx 50$ cm^{-1} [45]. Similar effects with different signs of λ were also observed in simpler antiferromagnetic systems FeF_2, MnF_2 [44], NiO [46], frustrated spinels [47], and some others.

IV. MAGNETIC STRUCTURE AND SPIN DYNAMICS

A. Magnetic structure

Reliable identification of the magnetic structure is essential for the analysis and understanding of physical properties, and in this section we will discuss it in the case of Ni_2NbBO_6.

Up to now, the magnetic structure was not determined experimentally, e.g., by neutron diffraction, but there are *ab initio* calculations which are supported by magnetostatic measurements [32]. For analyzing the magnetic symmetry, we will apply two techniques known as (i) the magnetic space group (MSG) analysis, and (ii) the irreducible representation analysis. The magnetic Ni^{2+} ions are placed inside the edge-shared oxygen octahedra and form armchairlike chains along the b axis. In its turn, these chains are corner-shared by [NiO_6] groups and interconnected by [BO_4] groups (see Fig. 1).

1. Magnetic space group analysis

The magnetic propagation vector for Ni_2NbBO_6 is still unknown and it is reasonable to assume a single k vector $\mathbf{k} = (0, 0, 0)$ structure, because most of the magnetics fall within this case [48]. This assumption, along with the known crystallographic space group and the site symmetry of Ni ions in the paramagnetic phase (see Table I), are sufficient for the symmetry analysis within the MSG approach with the use of the MAXMAGN code at the Bilbao crystallographic server [48]. There is no reason to assume that the magnetic group is lower then the k-maximal one, so we will perform the analysis with these assumptions.

The k-maximal magnetic subgroups for the chosen parent gray group are shown in Fig. 4. Images are visualized with the use of the VESTA program [49]. Since Ni^{2+} ions occupy the general 8d Wyckoff positions, with the lowest possible site symmetry (1), all eight possible magnetic groups can be realized. All derived magnetic space groups are centrosymmetric, thus no spontaneous electric polarization is expected. No splitting of atomic sites due to the magnetic ordering is predicted. The MSG index with respect to the parent group is two, hence only trivial AFM domains with opposite orientations of spins are expected.

2. Representation analysis

The representation analysis was applied to Ni_2NbBO_6 with the use of the ISODISTORT code [50]. The suggested magnetic propagation vector $\mathbf{k} = (0, 0, 0)$ corresponds to the Γ point in the Brillouin zone. Accordingly, eight one-dimensional irreducible representations (*irreps*) were found in total, each with three degrees of freedom. These corresponding irreducible representations are also depicted in Fig. 4. We note that in the case of the one-dimensional (1D) representations the results are completely equivalent to the MSG description.

3. Magnetic structure

Up to now, the exact magnetic structure of Ni_2NbBO_6 remains unknown, because no neutron or magnetic x-ray diffraction experiments were conducted. Nonetheless, the recently reported magnetostatic measurements point out a collinear antiferromagnetic structure with the AFM vector along the a axis; further *ab initio* calculations suggest a simple $\mathbf{k} = (0, 0, 0)$ structure [32]. According to our symmetry analysis presented above, the magnetic structure proposed in Ref. [32] was identified as a $Pn'ma'$ group in the MSG terms, or, equivalently, as a mGM4+ *irrep*. However, only four of the possible structures were tested by the DFT calculations in Ref. [32], whereas, as shown above, the eight possible magnetic subgroups could be realized in total. It is known that the application of the energy mapping analysis for determining

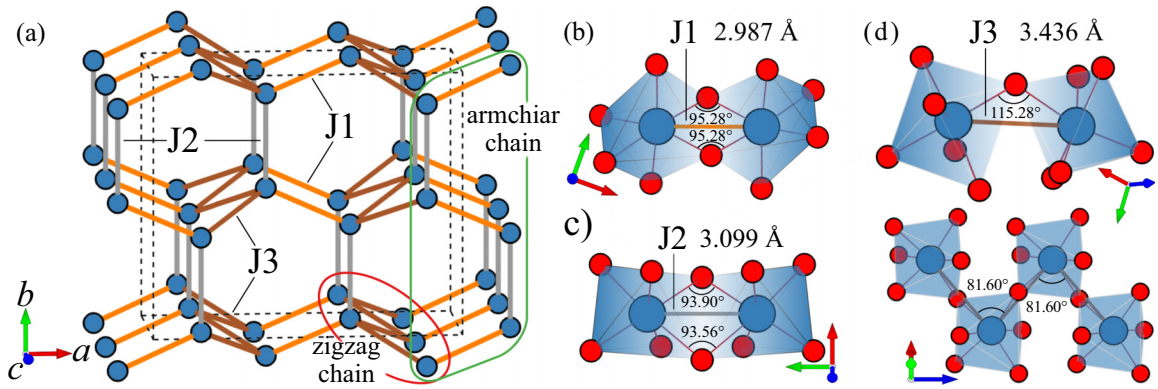

FIG. 5. (a) Crystal structure of Ni_2NbBO_6 (only Ni ions are shown) with up to the third neighbor exchanges. (b)–(d) Superexchange paths $J1$, $J2$, and $J3$ close-ups (oxygen ligands are shown) with corresponding Ni-Ni bond lengths and Ni-O-Ni bond angles. Zigzag chain formed by $J3$ superexchange is additionally shown in (d).

both the signs and magnitudes of exchange constants requires consideration of the full set of symmetry-inequivalent magnetic structures [51,52]. To this end, a more detailed analysis based on exchange paths and magnetic dynamics will be applied to further pursue the study of the magnetic structure of Ni_2NbBO_6.

The magnetic structure will be constructed using a minimal number of exchange paths to reproduce the 3D AFM properties of Ni_2NbBO_6. These superexchange interactions are shown in Fig. 5 where $J1$, $J2$, and $J3$ correspond to the first- (NN), second- (NNN), and third-nearest neighbor (NNNN) exchange paths, respectively. The $J1$ occurs through shared edges of $[NiO_6]$ octahedra consisting of two O^{2-} ions, with Ni-O and O-Ni distances of 2.016 45 and 2.026 46 Å, respectively. Ni-O-Ni bond angles for both oxygen ions are 95.28°. The $J2$ path occurs through a common edge of the two O^{2-} ions with O-Ni distances 2.120 35 and 2.126 29 Å, and Ni-O-Ni bond angles of 93.90° and 93.56°, respectively. The $J3$ exchange path is different, because it passes through a single oxygen ion, within the corner-shared octahedra. The Ni-O-Ni distances of 2.054 56 and 2.012 83 Å form the angle of 115.28° which noticeably deviates from 90°.

The well-known Goodenough-Kanamori-Anderson (GKA) rules [53,54] imply that the 90° superexchange pathway connecting partially filled $3d^8$ states of the two Ni^{2+} ions by the O^{2-} ions should be weak and ferromagnetic. Therefore, based on these structural peculiarities, the $J1$ and $J2$ exchange parameters should be ferromagnetic, while $J3$ is more likely to be antiferromagnetic. This exchange model is in disagreement with that suggested in [32]. The alternative, GKA compatible $Pn'm'a$ MSG (mGM2+ *irrep*), seems to be more plausible for the case of Ni_2NbBO_6. However, one should note that other subgroups, e.g., $[NbO_6]$ and $[BO_4]$ in our case, can lead to modification of the GKA rules, resulting in different magnitudes or even sign changes of exchange constants [55]. To resolve these uncertainties we have additionally taken into account the magnetic dynamics because not only static, but also the spin-excitation properties are dictated by the symmetry of the system; this will be described in the next section.

It is worth noting that the experimental values of the paramagnetic Curie temperature $\Theta = 9.5$ K and the Neél temperature $T_N = 23.5$ K [32] make it possible to calculate the frustration index $f = |\Theta|/T_N \approx 0.4$. The smallness of this value allows us to conclude that magnetic geometric frustrations in Ni_2NbBO_6 are small and can be neglected [56]. The exchange frustrations (within the three closest exchange paths model) can also be neglected since each set of these constants uniquely corresponds to magnetic structure (see Fig. 4). Exchange constants given in [32] can be used to calculate $\Theta = S(S+1)(J1 + J2 + 2J3)/3 = 11.91$ K, which is very close to the experimentally observed one.

As we noted above, an antiferromagnetic iron borate Fe_3BO_6 [57] also belongs to the same crystal structure in which Fe^{3+} ions occupy both $8d$ and $4c$ octahedral positions. The different occupation of $8d$ and $4c$ positions in Fe_3BO_6 and Ni_2NbBO_6 results in different sets of symmetry restrictions leading to completely different magnetic structures. Moreover, the dilution of the crystal structure by nonmagnetic Nb^{5+} ions in the $4c$ positions in Ni_2NbBO_6 leads to a drastic decrease of the magnetic ordering temperature from $T_N = 508$ K in Fe_3BO_6 [57,58] to $T_N = 23.5$ K in Ni_2NbBO_6. Evidently, such strong decrease is due to a different connectivity and noticeable difference between the spins $S = 1$ and $S = 5/2$ for Ni^{2+} and Fe^{3+}, respectively.

B. Magnetic scattering

Hereafter, manifestations of the magnetic Raman scattering will be discussed. Although the AFM transition temperature in Ni_2NbBO_6 is only $T_N = 23.5$ K, several spectral features unambiguously related to magnetic excitations were observed over the broad photon energy range up to 130 cm^{-1}, and up to the room temperature. Figure 6 summarizes experimental results of the low-frequency excitations observed in all required polarizations below and above T_N. According to literature, no structural transition is known in Ni_2NbBO_6 and this is additionally confirmed by our lattice-dynamics measurements (see Sec. III). Therefore, the structural mechanisms should be excluded from the discussion. Taking into account temperature dependences of the observed features which show strong correlations to T_N, they should definitely be assigned only to magnetic excitations.

The lowest-frequency feature is an intense quasielastic scattering (see Figs. 6 and 7), which is strongly quenched

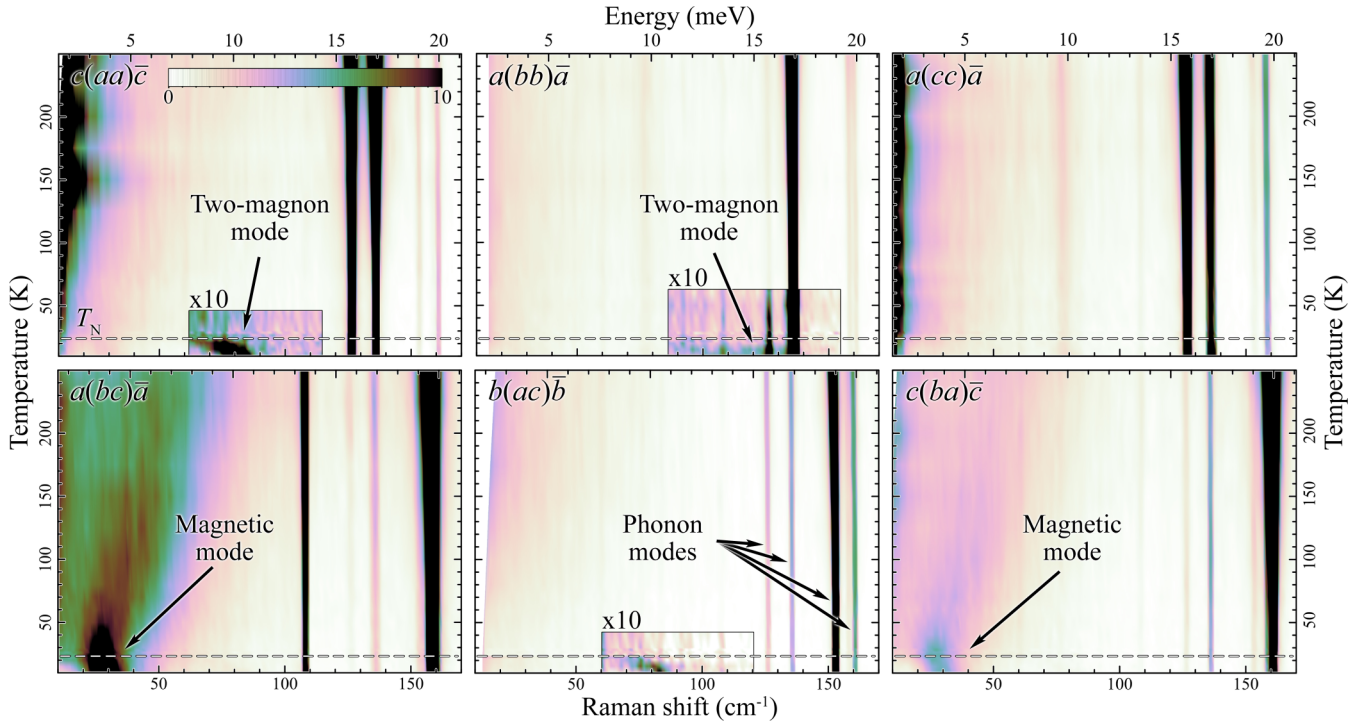

FIG. 6. Temperature dependences of the low-energy part of Raman-scattering spectra. Each panel corresponds to a specific polarization. The intensity scale is the same in all panels, except for the marked regions of interest with multiplied scale. A horizontal white-dashed line represents the AFM transition temperature. Note that the assumed spin-dimer mode possesses the highest intensity in the off-diagonal $a(bc)\bar{a}$ polarization, i.e., in the plane perpendicular to the antiferromagnetic vector.

in the magnetically ordered phase suggesting the presence of magnetic fluctuations above T_N. This shoulderlike contribution to the elastic band has a Lorentzian line shape which alludes to the mechanism of magnetic-energy-density fluctuations [59]. Its spectral weight can be additionally increased due to the well-pronounced spin-phonon interaction [60] (see Sec. III B) in Ni_2NbBO_6.

Next, there is an extremely intense and broad band at 30 cm^{-1} (at $T = 10$ K) observed only in the crossed $a(bc)\bar{a}$ and $c(ba)\bar{c}$ polarizations. Starting from the lowest temperature and up to T_N, this mode softens by 5 cm^{-1} without noticeable broadening. However, above T_N it shows strong hardening and becomes strongly damped (see Fig. 6). Remarkably, this excitation survives at temperatures up to 250 K ($\approx 10\,T_N$) as an extremely broad band without any noticeable loss of integral intensity. Nevertheless, we can definitely relate its origin to magnetic interactions due to the pronounced temperature dependence which correlates well with the AFM transition temperature.

It is interesting to remind one that a mode with very similar features such as the energy, half-width, and polarization properties was observed in another $S = 1$ nickel antiferromagnet $NiWO_4$ and was presumably assigned to either a Haldane gap mode or a dimer excitation [61]. It was appropriate to apply the Haldane gap model to $NiWO_4$ due to its magnetic structure consisting of coupled linear AFM chains of the $S = 1$ spins. However, the magnetic structure of Ni_2NbBO_6 is different from that of $NiWO_4$ and therefore the similar assignment cannot be directly applied to the observed mode. Temperature behavior, along with the spin-wave analysis given in Sec. IV C and in [61] make it possible to exclude both one- and two-magnon scattering. Even though at present the nature of this mode cannot be reliably identified, some scenarios can be suggested. Dimer excitations were previously observed in other systems, e.g., in $BiCu_2PO_6$ [62], but this system has a singlet ground state, which is very different from Ni_2NbBO_6, where magnetic susceptibility measurements clearly show the establishment of a long-range 3D-AFM ordering. Another hypothesis can be related to magnetoelastic excitations, since noticeable spin-phonon effects are observed on most phonons, or alternatively to a gapped magnetic fluctuation mode. It should be noted that a mode with similar behavior was also previously observed in a $S = 1/2$ system $Cu_4Te_5O_{12}Cl_4$ [63]. A perceptible effect of a resonance enhancement of the B_{3g} phonon at 109.1 cm^{-1} overlapping with this mode at $T > T_N$ is observed [see Fig. 7(c)].

Much weaker modes demonstrating different behavior were observed only in magnetically ordered phase below T_N in the $b(ac)\bar{b}$ and $a(bb)\bar{a}$ polarizations at 84.3 and 112.7 cm^{-1}, respectively (see Fig. 7). The half-widths of these excitations are much larger than phonon modes and their intensity is strongly temperature dependent. When the temperature rises, these modes lose intensity, rapidly broaden, and vanish at about T_N. Two possible scenarios can be suggested: (i) one-magnon excitations, more likely high-energy optical branches; and (ii) two-magnon (2M) modes. Characteristic marks of the one-magnon modes are their frequency dependence as a function of temperature which follows the Brillouin function [64]. However, the observed excitations manifest different behavior, namely, they do not soften down to zero energy with the

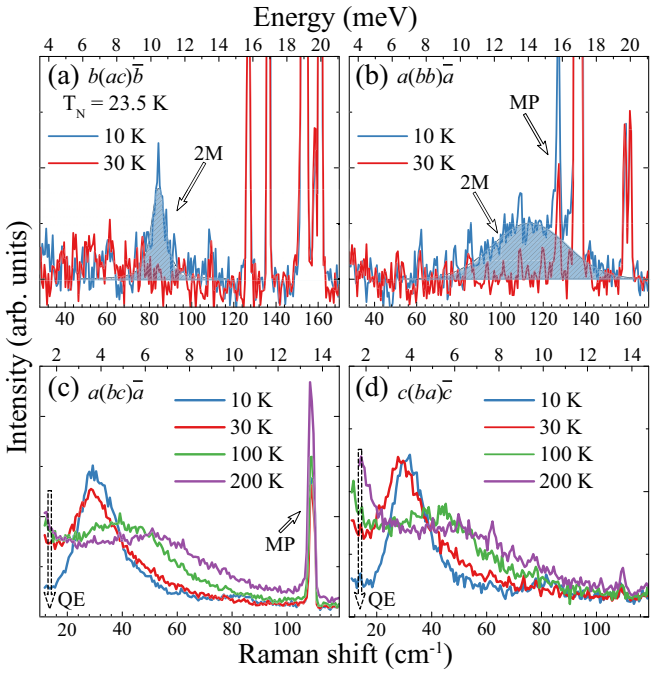

FIG. 7. (a),(b) Raman-scattering spectra for the $b(ac)\bar{b}$ and $a(bb)\bar{a}$ polarizations at temperatures below and above T_N. Two-magnon (2M) excitations are marked with arrows. Note the significant increase of the phonon-line intensity due to the magnon-phonon (MP) interaction in the region of their overlap. (c),(d) Raman-scattering spectra for the $a(bc)\bar{a}$ and $c(ba)\bar{c}$ polarizations at four temperatures. The magnetic mode at 30 cm^{-1} survives up to $\approx 10T_N$. Suppression of the quasielastic (QE) scattering in magnetically ordered phase due to the quenching of magnetic fluctuations can be clearly seen. The magnon-phonon interaction of this mode can be observed as well.

temperature increase. Moreover, both of these modes were registered in symmetrical polarizations [see Eq. (5)], which, in absence of anisotropic interactions, should be prohibited for the one-magnon scattering which must be purely antisymmetric in this case [64]. The above-mentioned observations make us recognize that these modes are indeed two-magnon excitations. We should note that in our measurements the temperature $T = 10$ K is only $\approx 0.6T_N$, which cannot be considered as a low-temperature limit in the case of $T_N = 23.5$ K and the thermal fluctuations should play an important role in damping of these modes. Another reason for broadening is the magnon-magnon interaction which is present even at the lowest temperatures. To confirm the validity of the suggested assignments of magnetic excitations, the spin-wave dispersion curves and the spin-wave density of states (DOS) should be calculated and this is done in the next section. As shown in Fig. 7(b), a similar effect of magnon-phonon interaction is manifested as enhancement of one of the A_g phonons at 127.2 cm^{-1} when it overlaps with the 2M mode at $T = 10$ K. Note that the leaking modes B_{3g} and B_{1g} at 158.8 and 161.2 cm^{-1} remain completely intact.

In most cases, the 2M modes correspond to excitations close to the Brillouin zone (BZ) boundaries, having short wavelengths. This means that such modes can be excited even in the absence of a long-range magnetic order at $T > T_N$. However, they are rapidly suppressed in Ni_2NbBO_6, possibly suggesting strong damping due to interaction with another excitation. For example, one such channel could be a low-energy 30 cm^{-1} mode, and this assumption is indirectly confirmed by the growth of its integral intensity with the temperature increase.

Polarization properties of all observed magnetic excitations are summarized in the form of the scattering matrices, as shown in Eq. (5). It should be noted that primed elements were written suggesting symmetric form of the tensors.

$$\begin{array}{c|c|c} \text{Mode} & \text{2M mode} & \text{2M mode} \\ 30\ \text{cm}^{-1} & 84.3\ \text{cm}^{-1} & 112.7\ \text{cm}^{-1} \\ \begin{pmatrix} 0 & ab' & 0 \\ ba & 0 & cb' \\ 0 & bc & 0 \end{pmatrix} & \begin{pmatrix} aa & 0 & ac \\ 0 & 0 & 0 \\ ca' & 0 & 0 \end{pmatrix} & \begin{pmatrix} 0 & 0 & 0 \\ 0 & bb & 0 \\ 0 & 0 & 0 \end{pmatrix}. \end{array} \tag{5}$$

C. Spin-wave calculations

Calculations of the spin-wave spectra and density of states within the linear spin-wave theory were done with the use of the SPINW library [65]. The following Hamiltonian was considered:

$$H = \sum_{\langle ij \rangle} J1 \cdot \mathbf{S}_i \cdot \mathbf{S}_j + \sum_{\langle ij \rangle} J2 \cdot \mathbf{S}_i \cdot \mathbf{S}_j + \sum_{\langle ij \rangle} J3 \cdot \mathbf{S}_i \cdot \mathbf{S}_j + \sum_i A S_i^{a2}, \tag{6}$$

where $J1$, $J2$, and $J3$ stand for isotropic exchange constants up to the third nearest neighbors with the values adopted from Ref. [32]. Magnetostatic measurements showed clear signs of the 3D long-range AFM transition and the spin-flop transition for the $H \parallel a$ axis [32]. We introduce an easy-axis anisotropy constant A along the same axis.

Results of the calculations are summarized in Fig. 8. There are eight magnetic Ni^{2+} ions in the unit cell that result in eight doubly degenerate spin-wave branches. Note the presence of crossing optical branches at the Γ-Z path, which can be interesting from the topological point of view [66].

The calculations predict that acoustic magnon mode (AFM resonance) has the frequency of 3.48 cm^{-1} (≈0.4314 meV), which is far below the achievable frequency range of our Raman-scattering setup (>10 cm^{-1}). No high-energy magnon excitations from optical spin-wave branches (at Γ) with energies of 4.742, 7.146, and 10.12 meV (38.25, 57.64, and 81.62 cm^{-1}) were observed in the Raman spectra. However, it is possible that the lowest of the optical magnons is overshadowed by a more intense and broad magnetic mode located at 30 cm^{-1}.

The two-magnon process consists of excitation of a pair of magnons with resulting total momentum $q = 0$ [67–69]. Thus, there is no restriction to momentum of individual magnons, and the resulting spectra should be proportional to the spin-wave density of states. Usually, the states near the BZ border give the most intense contribution to DOS, sometimes in the form of singular points (Van Hove singularities), because in most cases dispersion is nearly flat at the boundaries. The calculated DOS satisfactorily reproduces observations of two distinct modes. It seems that exchange constants should be larger in order to better reproduce the energy of the observed modes, with a

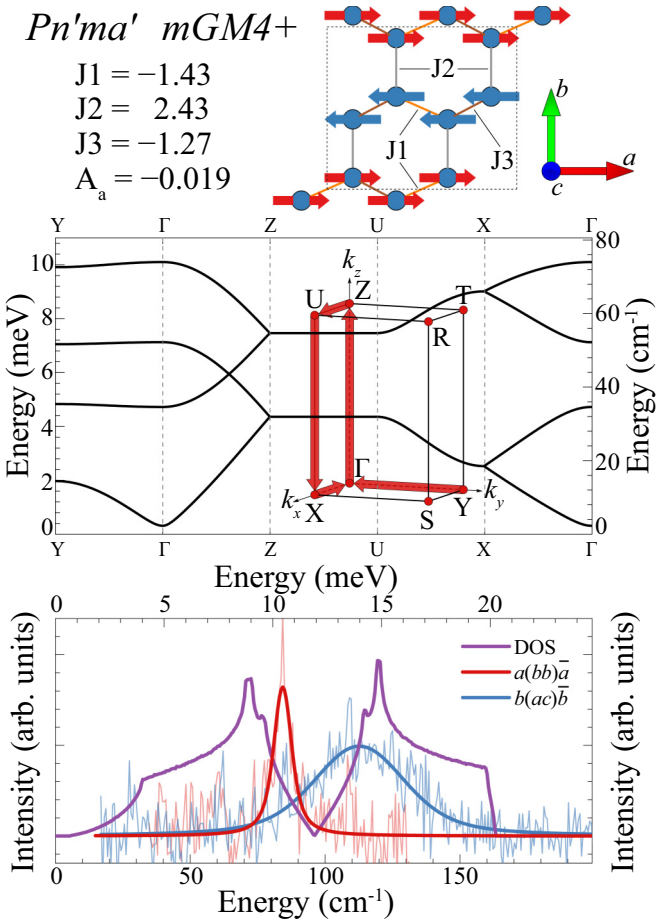

FIG. 8. Results of the LSWT calculations in comparison with experimental data (see text for details). Top: Set of exchange parameters (in meV) adopted from [32] and a sketch of the corresponding magnetic structure with a suggested MSG. Middle: Spin-wave dispersion curves calculated along the marked path in the Brillouin zone. Bottom: Experimentally observed two-magnon bands (at $T = 10$ K) in comparison with the calculated magnetic density of states (note that DOS energy is doubled in order to match the two-magnon process).

subsequent softening and damping due to magnon-magnon interactions. However, the theoretical description of these interactions is supposed to be very complicated due to the low symmetry of Ni_2NbBO_6, a large number of nonequivalent ions, and non-negligibility of all exchange interactions. The deviations from the low-temperature limit should be mentioned as another source of discrepancy between calculations and experiment.

A small value of the single-ion anisotropy constant A follows from the small value of the spin-flop field and therefore it is definitely not reliable to determine it from the comparison with 2M bands. The anisotropy only leads to a small linear shift of DOS. The A constant was determined by simulating the spin-flop transition in the applied magnetic field through mean-field calculations using a set of the exchange constants shown in Fig. 8. Calculations adopting such approach give $A = -0.019$ meV, reproducing the spin-flop transitions field of $\mu_0 H_{sf} = 3.67$ T [32].

The developed linear spin-wave model can explain only two 2M modes with energy 82 and 115 cm^{-1} out of the three experimentally registered magnetic excitations. The origin of the 30 cm^{-1} mode presently remains unexplained neither as a one-mode or a two-magnon mode. Further research is required with the use of either k-resolved techniques such as inelastic neutron or resonant x-ray scattering and/or other techniques susceptible to excitations of different parity such as infrared and terahertz spectroscopy. Moreover, complete understanding of the origin, energy, polarization, and temperature behavior of experimentally observed unusual magnetic excitations should be supported by more sophisticated theoretical models in applications to Ni_2NbBO_6.

V. CONCLUSIONS

In conclusion, magnetic and lattice dynamics of Ni_2NbBO_6 single crystals are studied with the use of the polarized Raman spectroscopy in the temperature range of 10–250 K. In total, 57 out of the 60 predicted Raman-active phonon modes were observed and reliably identified. Temperature dependences of observed phonon modes revealed an intense spin-phonon interaction manifested as hardening or softening of the particular phonons below T_N, suggesting strong coupling between the lattice and magnetic subsystems. A rich set of magnetic excitations was observed at 30, 84.3, and 112.7 cm^{-1} in the AFM phase and partly above the magnetic transition temperature with pronounced temperature dependences. While the nature of the low-energy mode remains unclear the two high-energy modes were identified as two-magnon excitations on the bases of their temperature/polarization behavior and calculations. Magnon dispersion curves with density of states were calculated within the linear spin-wave theory using the set of exchange parameters calculated in [32]. Our findings offer an opportunity for getting deeper insight into the magnetic dynamics of Ni_2NbBO_6 and provide a set of starting parameters for further investigations of spin dynamics, e.g., by inelastic neutron scattering or AFM resonance measurements. Magnetic symmetry analysis revealed that, in principle, all eight inequivalent possible magnetic subgroups should be taken into account for complete analysis of Ni_2NbBO_6 and isostructural antiferromagnets.

ACKNOWLEDGMENTS

The authors thank D. A. Andronikova for the help with x-ray orientation of single crystals and V. N. Gridnev for valuable comments. The experimental work was supported by Russian Science Foundation under the Project No. 16-12-10456. Crystal growth and LSWT calculations were supported by the joint Russian-Belorussian RFBR Projects No. 16-52-00127 and No. F16R-139.

[1] P. Lemmens, G. Güntherodt, and C. Gros, Magnetic light scattering in low-dimensional quantum spin systems, Phys. Rep. **375**, 1 (2003).

[2] I. Affleck, Quantum spin chains and the Haldane gap, J. Phys.: Condens. Matter **1**, 3047 (1989).

[3] W. J. L. Buyers, R. M. Morra, R. L. Armstrong, M. J. Hogan, P. Gerlach, and K. Hirakawa, Experimental evidence for the Haldane gap in a spin-1 nearly isotropic, antiferromagnetic chain, Phys. Rev. Lett. **56**, 371 (1986).

[4] T. Thio, T. R. Thurston, N. W. Preyer, P. J. Picone, M. A. Kastner, H. P. Jenssen, D. R. Gabbe, C. Y. Chen, R. J. Birgeneau, and A. Aharony, Antisymmetric exchange and its influence on the magnetic structure and conductivity of La_2CuO_4, Phys. Rev. B **38**, 905 (1988).

[5] S. H. Chun, J.-W. Kim, J. Kim, H. Zheng, C. C. Stoumpos, C. D. Malliakas, J. F. Mitchell, K. Mehlawat, Y. Singh, Y. Choi, T. Gog, A. Al-Zein, M. M. Sala, M. Krisch, J. Chaloupka, G. Jackeli, G. Khaliullin, and B. J. Kim, Direct evidence for dominant bond-directional interactions in a honeycomb lattice iridate Na_2IrO_3, Nat. Phys. **11**, 462 (2015).

[6] J. Reuther, R. Thomale, and S. Trebst, Finite-temperature phase diagram of the Heisenberg-Kitaev model, Phys. Rev. B **84**, 100406 (2011).

[7] J. S. Gardner, M. J. P. Gingras, and J. E. Greedan, Magnetic pyrochlore oxides, Rev. Mod. Phys. **82**, 53 (2010).

[8] J. E. Greedan, Geometrically frustrated magnetic materials, J. Mater. Chem. **11**, 37 (2001).

[9] S. H. Lee, C. Broholm, W. Ratcliff, G. Gasparovic, Q. Huang, T. H. Kim, and S. W. Cheong, Emergent excitations in a geometrically frustrated magnet, Nature (London) **418**, 856 (2002).

[10] A. Vasiliev, O. Volkova, E. Zvereva, and M. Markina, Milestones of low-D quantum magnetism, npj Quant. Mater. **3**, 18 (2018).

[11] M. Hagiwara, L. P. Regnault, A. Zheludev, A. Stunault, N. Metoki, T. Suzuki, S. Suga, K. Kakurai, Y. Koike, P. Vorderwisch, and J.-H. Chung, Spin Excitations in an Anisotropic Bond-Alternating Quantum S=1 Chain in a Magnetic Field: Contrast to Haldane Spin Chains, Phys. Rev. Lett. **94**, 177202 (2005).

[12] E. L. Nagaev, *Magnets with Complex Exchange Interactions* (Fizmatlit, Moscow, 1988).

[13] Z. Qiu, J. Li, D. Hou, E. Arenholz, A. T. N'Diaye, A. Tan, K.-i. Uchida, K. Sato, S. Okamoto, Y. Tserkovnyak, Z. Q. Qiu, and E. Saitoh, Spin-current probe for phase transition in an insulator, Nat. Commun. **7**, 12670 (2016).

[14] W. Lin, K. Chen, S. Zhang, and C. L. Chien, Enhancement of Thermally Injected Spin Current Through an Antiferromagnetic Insulator, Phys. Rev. Lett. **116**, 186601 (2016).

[15] H. Wang, C. Du, P. C. Hammel, and F. Yang, Antiferromagnonic Spin Transport from $Y_5Fe_5O_{12}$ into NiO, Phys. Rev. Lett. **113**, 097202 (2014).

[16] A. Qaiumzadeh, H. Skarsvåg, C. Holmqvist, and A. Brataas, Spin Superfluidity in Biaxial Antiferromagnetic Insulators, Phys. Rev. Lett. **118**, 137201 (2017).

[17] C. Song, Y. You, X. Chen, X. Zhou, Y. Wang, and F. Pan, How to manipulate magnetic states of antiferromagnets, Nanotechnology **29**, 112001 (2018).

[18] V. Baltz, A. Manchon, M. Tsoi, T. Moriyama, T. Ono, and Y. Tserkovnyak, Antiferromagnetic spintronics, Rev. Mod. Phys. **90**, 015005 (2018).

[19] E. V. Gomonay and V. M. Loktev, Spintronics of antiferromagnetic systems, Low Temp. Phys. **40**, 17 (2014).

[20] P. Němec, M. Fiebig, T. Kampfrath, and A. V. Kimel, Antiferromagnetic opto-spintronics, Nat. Phys. **14**, 229 (2018).

[21] C. Tzschaschel, K. Otani, R. Iida, T. Shimura, H. Ueda, S. Günther, M. Fiebig, and T. Satoh, Ultrafast optical excitation of coherent magnons in antiferromagnetic NiO, Phys. Rev. B **95**, 174407 (2017).

[22] T. P. Devereaux and R. Hackl, Inelastic light scattering from correlated electrons, Rev. Mod. Phys. **79**, 175 (2007).

[23] T. Moriya, Theory of absorption and scattering of light by magnetic crystals, J. Appl. Phys. **39**, 1042 (1968).

[24] Y. Rahnavard and W. Brenig, Spin dynamics of the anisotropic spin-1 antiferromagnetic chain at finite magnetic fields, Phys. Rev. B **91**, 054405 (2015).

[25] M. Sato, H. Katsura, and N. Nagaosa, Theory of Raman Scattering in One-Dimensional Quantum Spin-1/2 Antiferromagnets, Phys. Rev. Lett. **108**, 237401 (2012).

[26] M. G. Cottam and D. J. Lockwood, *Light Scattering in Magnetic Solids* (Wiley, New York, 1986).

[27] H. Gretarsson, N. H. Sung, M. Höppner, B. J. Kim, B. Keimer, and M. Le Tacon, Two-magnon Raman Scattering and Pseudospin-Lattice Interactions in Sr_2IrO_4 and $Sr_3Ir_2O_7$, Phys. Rev. Lett. **116**, 136401 (2016).

[28] T. M. H. Nguyen, L. J. Sandilands, C. H. Sohn, C. H. Kim, A. L. Wysocki, I.-S. Yang, S. J. Moon, J.-H. Ko, J. Yamaura, and Z. Hiroi, Two-magnon scattering in the 5*d* all-in-all-out pyrochlore magnet $Cd_2Os_2O_7$, Nat. Commun. **8**, 251 (2017).

[29] B. M. Wanklyn, F. R. Wondre, and W. Davison, Flux growth of crystals of some magnetic oxide materials: Mn_7SiO_{12}, CuO, MCr_2O_4, $MTiO_3$, Ni_2NbBO_6, $MMoO_4$ and $Li_2M_2(MoO)_4$, (M = Mn, Co, Ni), J. Mater. Sci. **11**, 1607 (1976).

[30] G. B. Ansell, M. E. Leonowicz, M. A. Modrick, B. M. Wanklyn, and F. R. Wondre, The structure of dinickel niobium (V) boron oxide Ni_2NbBO_6, Acta Crystallogr., Sect. B: Struct. Sci., Cryst. Eng. Mater. **38**, 892 (1982).

[31] R. Borromei and E. Cavalli, Low-temperature absorption spectrum of Ni^{2+} ion in single crystals of Ni_2NbBO_6, Phys. Status Solidi B **123**, 679 (1984).

[32] G. Narsinga Rao, V. N. Singh, R. Sankar, I. P. Muthuselvam, G.-Y. Guo, and F. C. Chou, Antiferromagnetism of Ni_2NbBO_6 with $S = 1$ dimer quasi-one-dimensional armchair chains, Phys. Rev. B **91**, 014423 (2015).

[33] R. V. Pisarev, M. A. Prosnikov, V. Y. Davydov, A. N. Smirnov, E. M. Roginskii, K. N. Boldyrev, A. D. Molchanova, M. N. Popova, M. B. Smirnov, and V. Y. Kazimirov, Lattice dynamics and a magnetic-structural phase transition in the nickel orthoborate $Ni_3(BO_3)_2$, Phys. Rev. B **93**, 134306 (2016).

[34] R. G. Burns, *Mineralogical Applications of Crystal Field Theory* (Cambridge University Press, Cambridge, UK, 1993), Vol. 5.

[35] A. B. P. Lever, *Inorganic Electronic Spectroscopy*, 2nd ed. (Elsevier, Amsterdam, 1984).

[36] J. Hugel and M. Belkhir, Nature of the NiO absorption edge within a spin polarized band scheme, Solid State Commun. **73**, 159 (1990).

[37] J. West and W. H. Taylor, The structure of norbergite, Z. Kristallogr. **70**, 461 (1929).

[38] N. V. Surovtsev and I. N. Kupriyanov, Temperature dependence of the Raman line width in diamond: Revisited, J. Raman Spectrosc. **46**, 171 (2015).

[39] M. Wojdyr, Fityk: a general-purpose peak fitting program, J. Appl. Crystallogr. **43**, 1126 (2010).

[40] L. Jun, X. Shuping, and G. Shiyang, FT-IR and Raman spectroscopic study of hydrated borates, Spectrochim. Acta, Part A **51**, 519 (1995).

[41] H. Navarro, J. E. Potts, and R. Merlin, Raman scattering from phonons and magnons in antiferromagnetic Fe_3BO_6, Solid State Commun. **50**, 331 (1984).

[42] M. Balkanski, R. F. Wallis, and E. Haro, Anharmonic effects in light scattering due to optical phonons in silicon, Phys. Rev. B **28**, 1928 (1983).

[43] T. Lan, X. Tang, and B. Fultz, Phonon anharmonicity of rutile TiO_2 studied by Raman spectrometry and molecular dynamics simulations, Phys. Rev. B **85**, 094305 (2012).

[44] D. J. Lockwood and M. G. Cottam, The spin-phonon interaction in FeF_2 and MnO_2 studied by Raman spectroscopy, J. Appl. Phys. **64**, 5876 (1988).

[45] X. K. Chen, J. C. Irwin, and J. P. Franck, Evidence for a strong spin-phonon interaction in cupric oxide, Phys. Rev. B **52**, R13130(R) (1995).

[46] E. Aytan, B. Debnath, F. Kargar, Y. Barlas, M. M. Lacerda, J. X. Li, R. K. Lake, J. Shi, and A. A. Balandin, Spin-phonon coupling in antiferromagnetic nickel oxide, Appl. Phys. Lett. **111**, 252402 (2017).

[47] T. Rudolf, C. Kant, F. Mayr, J. Hemberger, V. Tsurkan, and A. Loidl, Spin-phonon coupling in antiferromagnetic chromium spinels, New J. Phys. **9**, 76 (2007).

[48] J. M. Perez-Mato, S. V. Gallego, E. S. Tasci, L. Elcoro, G. de la Flor, and M. I. Aroyo, Symmetry-based computational tools for magnetic crystallography, Annu. Rev. Mater. Res. **45**, 217 (2015).

[49] K. Momma and F. Izumi, VESTA 3 for three-dimensional visualization of crystal, volumetric and morphology data, J. Appl. Crystallogr. **44**, 1272 (2011).

[50] B. J. Campbell, H. T. Stokes, D. E. Tanner, and D. M. Hatch, ISODISPLACE: a web-based tool for exploring structural distortions, J. Appl. Crystallogr. **39**, 607 (2006).

[51] H. Xiang, C. Lee, H.-J. Koo, X. Gong, and M.-H. Whangbo, Magnetic properties and energy-mapping analysis, Dalton Trans. **42**, 823 (2012).

[52] H.-J. Koo and M.-H. Whangbo, Density functional investigation of the magnetic properties of $PbMBO_4$ (M = Cr, Mn, Fe), Solid State Commun. **149**, 602 (2009).

[53] J. B. Goodenough, *Magnetism and the Chemical Bond* (Interscience, New York, 1963).

[54] S. V. Streltsov and D. I. Khomskii, Orbital physics in transition metal compounds: New trends, Phys. Usp. **60**, 1121 (2017).

[55] W. Geertsma and D. Khomskii, Influence of side groups on 90 superexchange: A modification of the Goodenough-Kanamori-Anderson rules, Phys. Rev. B **54**, 3011 (1996).

[56] P. Schiffer and A. P. Ramirez, Recent experimental progress in the study of geometrical magnetic frustration, Comments Condens. Matter Phys. **18**, 21 (1996).

[57] R. Diehl and G. Brandt, Refinement of the crystal structure of Fe_3BO_6, Acta Crystallogr., Sect. B: Struct. Sci., Cryst. Eng. Mater. **31**, 1662 (1975).

[58] C. Voigt and D. Bonnenberg, Temperature dependence of the magnetic susceptibility of Fe_3BO_6, Physica B&C (Amsterdam) **80**, 439 (1975).

[59] I. Yamada and H. Onda, Light scattering from magnetic-energy fluctuations in the one-dimensional Heisenberg antiferromagnet $KCuF_3$, Phys. Rev. B **49**, 1048 (1994).

[60] G. F. Reiter, Light scattering from energy fluctuations in magnetic insulators, Phys. Rev. B **13**, 169 (1976).

[61] M. A. Prosnikov, V. Y. Davydov, A. N. Smirnov, M. P. Volkov, R. V. Pisarev, P. Becker, and L. Bohatý, Lattice and spin dynamics in a low-symmetry antiferromagnet $NiWO_4$, Phys. Rev. B **96**, 014428 (2017).

[62] K.-Y. Choi, J. W. Hwang, P. Lemmens, D. Wulferding, G. J. Shu, and F. C. Chou, Evidence for Dimer Crystal Melting in the Frustrated Spin-Ladder System $BiCu_2PO_6$, Phys. Rev. Lett. **110**, 117204 (2013).

[63] K.-Y. Choi, S. Do, P. Lemmens, J. van Tol, J. Shin, G. S. Jeon, Y. Skourski, J.-S. Rhyee, and H. Berger, Coexistence of localized and collective magnetism in the coupled-spin-tetrahedra system $Cu_4Te_5O_{12}Cl_4$, Phys. Rev. B **90**, 184402 (2014).

[64] P. A. Fleury and R. Loudon, Scattering of light by one- and two-magnon excitations, Phys. Rev. **166**, 514 (1968).

[65] S. Toth and B. Lake, Linear spin wave theory for single-Q incommensurate magnetic structures, J. Phys.: Condens. Matter **27**, 166002 (2015).

[66] K. Li, C. Li, J. Hu, Y. Li, and C. Fang, Dirac and Nodal Line Magnons in Three-Dimensional Antiferromagnets, Phys. Rev. Lett. **119**, 247202 (2017).

[67] R. W. Davies, S. R. Chinn, and H. J. Zeiger, Spin-wave approach to two-magnon raman scattering in a simple antiferromagnet, Phys. Rev. B **4**, 992 (1971).

[68] S. R. Chinn, H. J. Zeiger, and J. R. O'Connor, Two-Magnon Raman Scattering in $KNiF_3$, J. Appl. Phys. **41**, 894 (1970).

[69] S. R. Chinn, H. J. Zeiger, and J. R. O'Connor, Two-Magnon Raman Scattering and Exchange Interactions in Antiferromagnetic $KNiF_3$ and K_2NiF_4 and Ferrimagnetic $RbNiF_3$, Phys. Rev. B **3**, 1709 (1971).